Circular Dichroism and Magnetic Circular Dichroism Studies of the Mixed-Valence Binuclear Non-Heme Iron Active Site in Uteroferrin and Its Anion Complexes

Yi-Shan Yang, James M. McCormick, and Edward I. Solomon*

Contribution from the Department of Chemistry, Stanford University, Stanford, California 94305

Received June 9, 1997[⊗]

Abstract: Uteroferrin (Uf) is a purple acid phosphatase for which the reduced [$Fe^{II}Fe^{III}$] form of the enzyme is catalytically active in the hydrolysis of phosphate esters. The binuclear non-heme iron active site of the native reduced enzyme (1/2metUf) and its molybdate- and phosphate-bound forms have been studied with absorption (ABS), circular dichorism (CD), and magnetic circular dichroism (MCD) spectroscopies to probe their geometric and electronic structure. CD and MCD in the UV−Vis region give the tyrosine (phenolate) to Fe^{III} charge transfer bands which probe the ferric center. CD and MCD in the NIR region probe the d−d transitions of both the Fe^{II} and the Fe^{III} centers. Variable-temperature variable-field (VTVH) MCD combined with EPR data are analyzed to determine the *g* values and energies of the ground state and the excited sublevels. These parameters are further interpreted in terms of a spin Hamiltonian model, which includes the zero-field splitting (ZFS) of Fe^{II} and Fe^{III} centers and the exchange coupling (*J*) between the irons due to bridging ligation. These ground and excited-state results confirm that both irons are six-coordinate with a μ-OH bridge. Anions bind to the active site in a bridging mode, which perturbs the ground and excited states of both iron centers. In particular, the exchange coupling decreases, μ-OH bridge → Fe^{II} bonding strength increases, and the Tyr → Fe^{III} donor interaction increases upon the phosphate binding. These results are correlated with the recent X-ray crystal structure of the kidney bean purple acid phosphatase, which contains an $Fe^{III}Zn^{II}$ active site. These studies provide geometric and electronic structure insight into the hydrolysis reaction mechanism of this enzyme.

Introduction

Binuclear non-heme iron proteins perform a variety of biological functions which often involve reactions with dioxygen. Members of this group of proteins include hemerythrin (Hr),[1,2] which is involved in oxygen transport and storage; ribonucleotide diphosphate reductase (RDPR),[3−5] which forms a catalytically active tyrosine radical; methane monooxygenase (MMO),[6−9] which activates dioxygen for insertion into carbon hydrogen bonds; acyl carrier protein Δ^9 desaturase (ACP Δ^9D),[10,11] which activates O_2 leading to the insertion of a 9,10 *cis* double bond in the conversion of stearoyl-ACP to oleyl-ACP; the purple acid phosphatases (PAP),[12−16] which catalyze the hydrolysis of phosphate esters; and rubrerythrin (Rb),[17] which still has an unclear function. The binuclear site can have three oxidation states including met [$Fe^{III}Fe^{III}$], 1/2met (or semimet) [$Fe^{II}Fe^{III}$], and fully reduced [$Fe^{II}Fe^{II}$]. All three oxidation states can be obtained for Hr, MMO, and RDPR. PAP has only been found in the met and 1/2met forms, and it is the only enzyme which is active in the 1/2met form.

Phosphate esters are important intermediary metabolites.[18] A variety of phosphatases catalyze the hydrolysis of these esters.[19−21] Acid phosphatases have optimal activities at pH $\leq \sim 6.0$.[22] Many phosphatases whose hydrolysis reactions have been studied have been found to function via a three-step mechanism (eq 1),

$$E + ROHPO_3^- \leftrightarrow E^*ROHPO_3^- \rightarrow E-PO_3^- \rightarrow E + H_2PO_4^- \quad (1)$$

which involves the formation of a covalent phosphoenzyme. However, the relevance of this mechanism to the acid phosphatases must still be elucidated.

Purple acid phosphatases (PAPs) catalyze the hydrolysis of certain phosphate esters including arylphosphates, di- and

[⊗] Abstract published in *Advance ACS Abstracts,* November 1, 1997.

(1) Wilkins, P. C.; Wilkins, R. G. *Coord. Chem. Rev* **1987**, *79*, 195−214.
(2) Klotz, I. M.; Kurtz, D. M. *Acc. Chem. Res* **1984**, *17*, 16−22.
(3) Stubbe, J. A. *J. Biol. Chem.* **1990**, *265*, 5329−5332.
(4) Nordlund, P.; Eklund, H. *J. Mol. Biol.* **1993**, *232*, 123−164.
(5) Reichard, P.; Ehrenberg, A. *Science* **1983**, *221*, 514−519.
(6) Lipscomb, J. D. *Annu. Rev. Microbiol.* **1994**, *48*, 371−399.
(7) Froland, W. A.; Andersson, K. K.; Lee, S.-K.; Liu, Y.; Lipscomb, J. D. In *Microbial Growth on C_1 Compounds*; Myrrell, J. C., Kelly, D. P., Eds.; Intercept Ltd.: Andover, 1993; pp 81−92.
(8) Fox, B. G.; Lipscomb, J. D. In *Biological Oxidation Systems*; Reddy, C. C., Hamilton, G. A., Madyastha, K. M., Eds.; Academic Press: New York, 1992; Vol. 1, pp 367−388.
(9) Dalton, H. In *Advances in Applied Microbiology*; Umbreit, W. W., Ed.; Academic Press: New York, 1980; Vol. 26, pp 71−87.
(10) Fox, B. G.; Shanklin, J.; Somerville, C.; Münck, E. *Proc. Natl. Acad. Sci., U.S.A.* **1993**, *90*, 2486−2490.
(11) Fox, B. G.; Shanklin, J.; Ai, J.; Loehr, T. M.; Sanders-Loehr, J. *Biochemistry* **1994**, *33*, 12776−12786.
(12) Doi, K.; Antanaitis, B. C.; Aisen, P. In *Structure and Bonding*; Clarke, M. J., Goodenough, J. B., Ibers, J. A., Jorgensen, C. K., Mingos, D. M. P., Neilands, J. B., Palmer, G. A., Reinen, D., Sadler, P. J., Weiss, R., Williams, R. J. P., Eds.; Springer-Verlag: Heidelberg, 1988; Vol. 70, pp 1−26.
(13) Vincent, J. B.; Averill, B. A. *FASEB J.* **1990**, *4*, 3009−3014.
(14) Antanaitis, B. C.; Aisen, P. In *Frontiers in Bioinorganic Chemistry*; Xavier, A. V., Ed.; VCH: New York, 1986; pp 481−493.
(15) Que, L., Jr.; Scarrow, R. C. In *Metal Clusters in Proteins*; Que, L., Ed.; American Chemical Society: Washington, DC, 1988; pp 152−178.
(16) Vincent, J. B.; Olivier-Lilley, G. L.; Averill, B. A. *Chem. Rev.* **1990**, *90*, 1447-1467.
(17) LeGall, B. G.; Prickril, B. C.; Moura, I.; Xavier, A. V. *Biochemistry* **1988**, *27*, 1636−1642.
(18) Westheimer, F. H. *Chem. Rev.* **1981**, *81*, 313−326.
(19) Egloff, M.-P.; Cohen, P. T. W.; Reinemer, P.; Barford, D. *J. Mol. Biol.* **1995**, *254*, 942−959.
(20) Griffith, J. P.; Kim, J. L.; Kim, E. E.; Sintchak, M. D.; Thomson, J. A.; Fitzgibbon, M. J.; Fleming, M. A.; Caron, P. R.; Hsiao, K.; Navia, M. A. *Cell* **1995**, *82*, 507−522.
(21) Kim, E. E.; Wyckoff, H. W. *J. Mol. Biol.* **1991**, *218*, 449−464.
(22) Aquino, M. A. S.; Lim, J.-S.; Sykes, A. G. *J. Chem. Soc., Dalton Trans.* **1994**, 429−436.

S0002-7863(97)01896-9 CCC: $14.00

triphosphonucleotides, phosphoserine, phosphothreonine, and phosphotyrosine proteins. They have been isolated from a variety of animal and plant sources, with the best characterized enzymes isolated from kidney beans (KBPAP),[23,24] bovine spleen (BSPAP),[25−27] and porcine uterus (uteroferrin, Uf).[28−30] KBPAP has a $Zn^{II}Fe^{III}$ active center while BSPAP and Uf have a binuclear $Fe^{II}Fe^{III}$ active center. There is 90% sequence homology between Uf and BSPAP.[31,32] On the basis of EPR, Mössbauer, and magnetic susceptibility studies,[26,33−38] the two mammalian enzymes contain an antiferromagnetically coupled binuclear iron site. Mammalian PAP can be obtained in two oxidation states. The purple oxidized ($Fe^{III}Fe^{III}$, met) form is catalytically inactive and EPR silent with a maximum absorption at 550 nm (ϵ = 4000 M^{-1} cm^{-1}). The exchange coupling constant has been estimated to be between 80 and 300 cm^{-1}, which indicates strong antiferromagnetic coupling between the two irons. The pink reduced ($Fe^{II}Fe^{III}$, half-met) form is catalytically active. It has an absorption maximum shifted to 510 nm (ϵ = 4000 M^{-1} cm^{-1}) and EPR g values at 1.94, 1.76, and 1.56.[29,33,36,39−41] The latter result from antiferromagnetic coupling between the high-spin ferric ion and the high-spin ferrous ion to give an $S_{tot} = {}^1/_2$ ground state. The exchange coupling constant of the $Fe^{III}Fe^{II}$ center is $-J > \sim 5$ cm^{-1} for $H = -2JS_1 \cdot S_2$,[34−38] which indicates that 1/2metUf has a hydroxo bridge similar to other mixed valence binuclear iron systems such as 1/2methemerythrin. Endogenous ligands at the binuclear site have been identified by a combination of spectroscopic methods, including Abs, NMR, EXAFS, resonance Raman, Mössbauer, NOESY, ESEEM, and ENDOR. Uteroferrin's unique purple color derives from a charge transfer transition from the tyrosine ligand to the ferric center as demonstrated by resonance Raman spectroscopy.[28,35,47] Features assigned to an Fe^{III}-bound tyrosinate are also observed in the ^{1}H NMR spectrum.[42−44] No dramatic change is observed in Abs and resonance Raman spectroscopy upon 1-electron reduction of the met derivatives, which implies that the tyrosine ligand binds to only the ferric center.[27 28,30,35,47,55] ^{1}H NMR,[42−44] ENDOR,[49,50] and NOESY[48] spectroscopic studies on uteroferrin provide evidence for His coordination. ^{1}H NMR[42−44,48−50] and Mössbauer[33−35,37] suggest that there are also carboxylate ligands.

Several oxoanions are inhibitors of uteroferrin.[42,45,51,52] Phosphate (PO_4^{3-})[22,53−56] and arsenate (AsO_4^{3-})[22,45,56] are competitive inhibitors which lower the reduction potential[57] and lead to aerobic oxidation of the site to the inactive met level.[51] Magnetic susceptibility studies show that 1/2metUf has a much weaker antiferromagnetic coupling between the metal sites after the phosphate binding[36,38] and a dramatically altered EPR signal that is broad and difficult to observe.[31,36,56] Molybdate (MoO_4^{2-})[49,74] and tungstate (WO_4^{2-})[74] are noncompetitive inhibitors, which are thought to interact with the active site in a different manner due to their much larger binding constants.[27,55] These anions increase the reduction potential and stabilize the half-met site.[57] They produce a more limited change in the ground state spectral features (molybdate changes the EPR spectrum from rhombic to axial).

KBPAP, another well-studied purple acid phosphatase from plants, has one Fe^{III} and one Zn^{II} in the active center. Recent X-ray crystallographic structures[58,59] of resting KBPAP (Figure 1) and the oxoanion-bound derivatives indicate that the iron is coordinated by Tyr167, His325, and Asp135; the zinc is coordinated by His286, His323, and Asn201. The two metals are bridged by the carboxylate group of Asp164. Three exogenous ligands are also included in the X-ray model to complete the coordination sphere: one terminal hydroxo ligand to iron, one terminal water ligand to zinc, and one μ-hydroxo bridge between the metal ions. Oxoanions interact with one oxygen atom of each metal, replacing two modeled water derived solvent ligands, and bind via a bridging mode. The $Fe^{III}Zn^{II}$ center can be converted to an $Fe^{II}Fe^{III}$ form[60−62] that

(23) Beck, J. L.; McConachie, L. A.; Summors, A. C.; Arnold, W. N.; de Jersey, J.; Zerner, B. *Biochim. Biophys. Acta* **1986**, *869*, 61−68.
(24) Beck, J. L.; de Jersey, J.; Zerner, B. *J. Am. Chem. Soc.* **1988**, *110*, 3317−3318.
(25) Orlando, J. L.; Zirino, T.; Quirk, B. J.; Averill, B. A. *Biochemistry* **1993**, *32*, 8120−8129.
(26) Davis, J. C.; Averill, B. A. *Proc. Natl. Acad. Sci. U.S.A.* **1982**, *79*, 4623−4627.
(27) Dietrich, M.; Münstermann, D.; Suerbaum, H.; Witzel, H. *Eur. J. Biochem.* **1991**, *199*, 105−113.
(28) Antanaitis, B. C.; Strekas, T.; Aisen, P. *J. Biol. Chem.* **1982**, *257*, 3766−3770.
(29) Antanaitis, B. C.; Aisen, P.; Lilienthal, H. R. *J. Biol. Chem.* **1983**, *258*, 3166-3172.
(30) Antanaitis, B. C.; Aisen, P. In *Advanced Inorganic Biochemistry*; Theil, E. C., Eichhorn, G. L., Marzilli, L. G., Eds.; Elsevier: 1983; Vol. 5, pp 111−136.
(31) Hunt, D. F.; Yates, J. R., III; Shabanowitz, J.; Zhu, N.-Z.; Zirino, T.; Averill, B. A.; Daurat-Larroque, S. T.; Shewale, J. G.; Roberts, R. M.; Brew, K. *Biochem. Biophys. Res. Commun.* **1987**, *144*, 1154−1160.
(32) Ketcham, C. M.; Roberts, R. M.; Simen, C. M.; Nicke, H. S. *J. Biol. Chem.* **1989**, *264*, 557−563.
(33) Debrunner, P. G.; Hendrich, M. P.; de Jersey, J.; Keough, D. T.; Sage, J. T.; Zerner, B. *Biochim. Biophys. Acta* **1983**, *745*, 103−106.
(34) Sage, J. T.; Xia, Y.-M.; Debrunner, P. G.; Keough, D. T.; de Jersey, J.; Zerner, B. *J. Am. Chem. Soc.* **1989**, *111*, 7239−7247.
(35) Averill, B. A.; Davis, J. C.; Burman, S.; Zirino, T.; Sanders-Loehr, J.; Loehr, T. M.; Sage, J. T.; Debrunner, P. G. *J. Am. Chem. Soc.* **1987**, *109*, 3760−3767.
(36) Day, E. P.; David, S. S.; Peterson, J.; Dunham, W. R.; Bonvoisin, J. J.; Sands, R. H.; Que, L., Jr. *J. Biol. Chem.* **1988**, *263*, 15561−15567.
(37) Rodriguez, J. H.; Ok, H. N.; Xia, Y.-M.; Debrunner, P. G.; Hinrichs, B. E.; Meyer, T.; Packard, N. H. *J. Phys. Chem.* **1996**, *100*, 6849−6862.
(38) Gehring, S.; Behlendorf, M.; Fleischhauer, P.; Hüber, M.; Lorösch, J.; Haase, W.; Dietrich, M.; Witzel, H.; Löcke, R.; Krebs, B. *Inorg. Chim. Acta* **1996**, *252*, 13−17.
(39) Antanaitis, B. C.; Aisen, P.; Lilienthal, H. R.; Roberts, R. M.; Bazer, F. W. *J. Biol. Chem.* **1980**, *255*, 11204−11209.
(40) Antanaitis, B. C.; Aisen, P. *J. Biol. Chem.* **1982**, *257*, 1855−1859.
(41) Antanaitis, B. C.; Aisen, P. *J. Biol. Chem.* **1982**, *257*, 5330−5332.
(42) Scarrow, R. C.; Pyrz, J. W.; Que, L., Jr. *J. Am. Chem. Soc.* **1990**, *112*, 657−665.
(43) Lauffer, R. B.; Antanaitis, B. C.; Aisen, P.; Que, L., Jr. *J. Biol. Chem.* **1983**, *258*, 14212−14218.
(44) Wang, Z.; Ming, L.-J.; Que, L., Jr.; Vincent, J. B.; Crowder, M. W.; Averill, B. A. *Biochemistry* **1992**, *31*, 5263−5268.
(45) True, A. E.; Scarrow, R. C.; Randall, C. R.; Holz, R. C.; Que, L., Jr. *J. Am. Chem. Soc.* **1993**, *115*, 4246−4255.
(46) Wang, X.; Randall, C. R.; True, A. E.; Que, L., Jr. *Biochemistry* **1996**, *35*, 13946−13954.
(47) Gaber, B. P.; Sheridan, J. P.; Bazer, F. W.; Roberts, R. M. *J. Biol. Chem.* **1979**, *254*, 8340−8342.
(48) Holz, R. C.; Que, L., Jr.; Ming, L.-J. *J. Am. Chem. Soc.* **1992**, *114*, 4434−4436.
(49) Doi, K.; McCracken, J.; Peisach, J.; Aisen, P. *J. Biol. Chem.* **1988**, *263*, 5757−5763.
(50) Antanaitis, B. C.; Peisach, J.; Mims, W. B.; Aisen, P. *J. Biol. Chem.* **1985**, *260*, 4572−4574.
(51) Antanaitis, B. C.; Aisen, P. *J. Biol. Chem.* **1985**, *260*, 751−756.
(52) Crans, D. C.; Simone, C. M.; Holz, R. C.; Que, L., Jr. *Biochemistry* **1992**, *31*, 11731−11739.
(53) Keough, D. T.; Beck, J. L.; de Jersey, J.; Zerner, B. *Biochem. Biophys. Res. Commun.* **1982**, *108*, 1643−1648.
(54) Doi, K.; Gupta, R.; Aisen, P. *J. Biol. Chem.* **1987**, *262*, 6982−6985.
(55) Pyrz, J. W.; Sage, J. T.; Debrunner, P. G.; Que, L., Jr. *J. Biol. Chem.* **1986**, *261*, 11015−11020.
(56) David, S. S.; Que, L., Jr. *J. Am. Chem. Soc.* **1990**, *112*, 6455−6463.
(57) Wang, D. L.; Holz, R. C.; David, S. S.; Que, L., Jr.; Stankovich, M. T. *Biochemistry* **1991**, *30*, 8187−8194.
(58) Sträter, N.; Klabunde, T.; Tucker, P.; Witzel, H.; Krebs, B. *Science* **1995**, *268*, 1489−1492.
(59) Klabunde, T.; Sträter, N.; Frîhlich, R.; Witzel, H.; Krebs, B. *J. Mol. Biol.* **1996**, *259*, 737−748.
(60) Beck, J. L.; McArthur, M. J.; de Jersey, J.; Zerner, B. *Inorg. Chim. Acta* **1988**, *153*, 39−44.
(61) Beck, J. L.; Keough, D. T.; de Jersey, J.; Zerner, B. *Biochim. Biophys. Acta.* **1984**, *791*, 357−363.

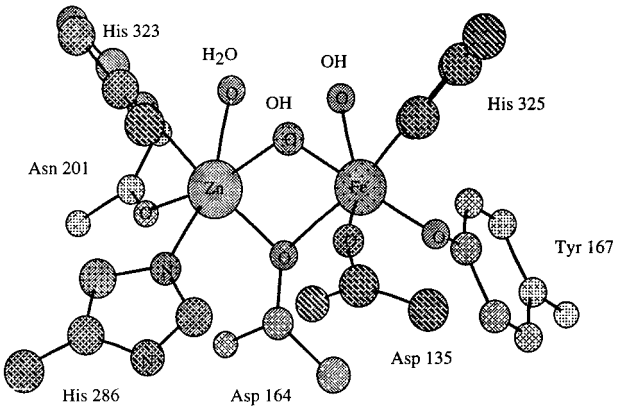

Figure 1. Schematic representation of the crystallographically determined binuclear $Fe^{III}-Zn^{II}$ active site of kidney bean purple acid phosphatase.

is also catalytically active. The EPR, Mössbauer, and resonance Raman spectra of this site are similar to those of 1/2metUf, indicating that these enzymes have similar active sites with a similar ligand environment.[24,56,62]

Non-heme ferrous sites have been difficult to study as they are not easily accessible through the usual methods of EPR and absorption. However, a combination of circular dichroism (CD), magnetic circular dichroism (MCD), and variable-temperature variable-field (VTVH) MCD provide a spectroscopic protocol for the study of ferrous active sites in non-heme metalloenzymes. This combination of spectroscopies based on different selection rules allows observation of weak electronic transitions to ligand field excited states. The temperature and field dependence of these bands in MCD further probes the ground state splittings of the ferrous center. High-spin d^6 Fe^{II} in an octahedral ligand field has a $^5T_{2g}$ ground state with a ^5E_g excited state at $10Dq_{oh}$ ($\sim$10 000 cm^{-1}). Low site symmetry effects split the ^5E_g excited state (Δ^5E) by up to $\sim$2000 cm^{-1}. In five-coordinate geometries the ^5E_g state splitting increases, with $\Delta^5E \geq \sim$5000 cm^{-1}. For tetrahedral ferrous coordination $10Dq_{Td}$ is $(-4/9)(10Dq_{Oh})$, which results in ligand field transitions at $\sim$5000 cm^{-1}.

All ligand field transitions of high-spin Fe^{III} are spin forbidden and weak in Abs. However, these can increase in intensity when close in energy to intense charge transfer transitions. The lowest energy high-spin Fe^{III} ligand field transitions are $^6A_1 \rightarrow {}^4T_1$ and $^6A_1 \rightarrow {}^4T_2$, which decrease in energy with increase in coordination number:[63] tetrahedral geometries ($^6A_1 \rightarrow {}^4T_1$ 16500−18100 cm^{-1}, $^6A_1 \rightarrow {}^4T_2$ 19900−20900 cm^{-1}), five-coordinate geometries ($^6A_1 \rightarrow {}^4T_1$ 7500−14000 cm^{-1}, $^6A_1 \rightarrow {}^4T_2$ 16100−20100 cm^{-1}), and octahedral geometries ($^6A_1 \rightarrow {}^4T_1$ 7200−11400 cm^{-1}, $^6A_1 \rightarrow {}^4T_2$ 12000−15800 cm^{-1}). Alternatively, ferric complexes often exhibit intense LMCT transitions, which probe the electronic structure of the ferric site. Analysis of the ligand field and charge transfer spectral features of 1/2metUf allows construction of an experimental ligand field energy level diagram for the ferrous and ferric sites, which provides insight into their geometric and electronic structure.

In this study the iron centers in the 1/2metUf active site are studied with a combination of excited-state spectral methods (ABS, CD, and LTMCD) in both the ligand field region from 6000 to $\sim$18000 cm^{-1} and the LMCT region from $\sim$18000 to $\sim$33000 cm^{-1}. The dimer ground-state magnetic structure has been determined by VTVH MCD and spin Hamiltonian analysis. Together, these methods provide a direct probe of the geometric and electronic structure of both the ferrous and ferric sites as well as the interactions between the metal centers in the dimer. These studies have been performed on 1/2metUf, 1/2metUf-MoO_4, and 1/2metUfPO_4. The results obtained provide significant insight into the geometric and electronic structure contributions to the catalytic mechanism of the active site.

Experimental Section

Uteroferrin was isolated and purified according to literature procedures.[64] Purified Uf with $A_{280}/A_{550} < 14$ was dialyzed against a 0.1 M sodium acetate buffer at pH 4.9 and frozen in liquid N_2 for subsequent use. The protein is isolated in the inactive $Fe^{III}Fe^{III}$ met form with phosphate tightly bound. The bound phosphate could be removed by reduction to 1/2metUf. 1/2metUf was prepared from metUfPO_4 by either of two methods. (1) Approximately 1 mM metUfPO_4 was incubated at 4 °C for 24 h with 100 mM 2-mercaptoethanol and catalytic amounts of Fe^{2+} (as ferrous ammonium sulfate). The enzyme was then passed through a 1 × 6 cm Sephadex G25 column that had been equilibrated with 0.1 M pH 4.9 sodium acetate buffer. (2) metUfPO_4 was dialyzed anaerobically at 4 °C for 24 h against the 0.1 M pH 4.9 acetate buffer that was 100 mM in 2-mercaptoethanol and a catalytic amount of Fe^{2+} (as ferrous ammonium sulfate), followed by several changes of anaerobic buffer. 1/2metUf samples obtained by either method were identical. The concentration was measured from the absorbances at 280 (ϵ = 50 000 M^{-1} cm^{-1}) and 515 nm (ϵ = 4000 M^{-1} cm^{-1}).

The oxoanion-bound forms of 1/2metUf were prepared by anaerobic addition of anion solution (50 mM of MoO_4^{2-} and 3.3 M of PO_4^{3-}) in 0.1 M pH 4.9 acetate buffer to $\sim$1 to 2.5 mM anaerobic 1/2metUf (prepared by anaerobic dialysis for $\sim$24 h at 4 °C). For 1/2metUfMoO_4, $\sim$1.1 to 2.0 molar equiv were added, and for 1/2metUfPO_4, the final concentration of PO_4^{3-} was 100−150 mM. Helium temperature EPR spectra for 1/2metUf and its derivatives were used to detect the extent of reduction from met form and conversion to the anion-bound forms.[24−27,29,33,35−36,39−41,51,56,69] MetUf samples were prepared by oxidation of the corresponding 1/2met derivatives with >10-fold molar excess of H_2O_2. The UV−vis solution absorbance spectra were obtained with a Cary-17 spectrometer. Circular dichroism studies were performed on a JASCO J-500 spectropolarimeter operating with the S-20 photomultiplier in the 900−300-nm region. Low-temperature magnetic circular dichroism data were acquired with the same spectropolarimeter, equipped with an Oxford Instruments SM4-7T superconducting magnet capable of magnetic fields up to 7.0 T and temperatures down to 1.6 K. CD and MCD spectra from 600 to 2000 nm were obtained on a JASCO J200D spectropolarimeter equipped with an Oxford Instrument SM4000-7T superconducting magnet. A Bruker ER 200D-SRC EPR equipped with an Air Products L2R-110 He cryostat was used to obtained the EPR spectra.

Protein samples (2.0 mM for the near-IR region and 1.5 mM for the UV−vis region) were prepared for MCD studies by mixing with 66% glycerol-d_3 pD 4.9. EPR spectra showed no significant change with the addition of glycerol. The samples were slowly inserted into the cryostat to reduce the strain of the resulting frozen optical glass. The depolarization of the protein glass was checked by measuring the CD

(62) Suerbaum, H.; Körner, M.; Witzel, H.; Althaus, E.; Mosel, B.-D.; Müller-Warmuth, W. *Eur. J. Biochem* **1993**, *214*, 313−321.
(63) Zhang, Y.; Gebhard, M. S.; Solomon, E. I. *J. Am. Chem. Soc.* **1991**, *113*, 5162−5175.
(64) Basha, S. M. M.; Bazer, F. W.; Geisert, R. D.; Roberts, R. M. *J. Anim. Sci.* **1980**, *50*, 113−123.
(65) The MCD spectra were fit first. The parameters obtained were then applied to the CD and Abs spectra, with the peak position allowed to vary within $\sim\pm$300 cm^{-1}, the band width was allowed to increase for room temperature Abs and 5 °C CD data, and the peak height was allowed to float. High-energy Abs bands (E > 28 000 cm^{-1}) were allowed to increase the band width due to their being on the shoulder region.
(66) Bennett, D. E.; Johnson, M. K. *Biochim. Biophys. Acta* **1987**, *911*, 71−80.
(67) Browett, W. R.; Fucaloro, A. F.; Morgan, T. V.; Stephens, P. J. *J. Am. Chem. Soc.* **1983**, *105*, 1868−1872.
(68) Solomon, E. I.; Pavel, E. G.; Loeb, K. E.; Campochiaro, C. *Coord. Chem. Rev.* **1995,** *144*, 369−460.
(69) McCormick, J. M.; Reem, R. C.; Solomon, E. I. *J. Am. Chem. Soc.* **1991**, *113*, 9066−9079.
(70) Crowder, M. W.; Vincent, J. B.; Averill, B. A. *Biochemistry* **1992**, *31*, 9603−9608.

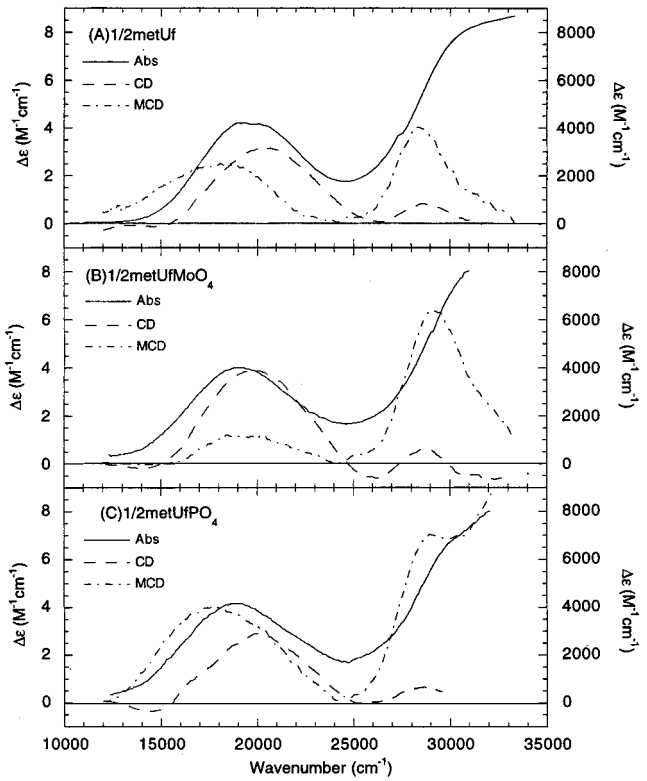

Figure 2. Abs (—), CD (- - -), and LT MCD (-·-) spectra of the binuclear non-heme $Fe^{II}Fe^{III}$ active site of uteroferrin in the charge transfer region: (A) 1/2metUf, (B) 1/2metUfMoO_4, and (C) 1/2metUf-PO_4. The Abs, CD, and low-temperature MCD spectra were recorded at room temperature, 5 °C, and 5K/7T, respectively.

spectrum of a freshly prepared nickel tartrate solution placed immediately before and after the MCD sample.

Abs, CD, and MCD spectra were fit to Gaussian band shapes by using a constrained nonlinear least-squares fitting procedure. Each spectroscopic method has different selection rules, thus transitions can have different intensities and different signs, while the energies and band widths are the same. The MCD spectra are taken at low temperature, thus they may have significantly sharper band widths and the band energies may shift slightly relative to the room temperature Abs and CD data, which was allowed for in the final fit. VTVH MCD and 1/*T* MCD data (MCD intensity, temperature, and the applied magnetic field) were fit by using a simplex routine which minimizes the χ^2 value. A goodness-of-fit parameter (χ^2/number of float parameters) was utilized for the comparison of different fit results.

Results and Analysis

A. Charge Transfer Transition Region. Figure 2 shows the Abs, CD, and MCD spectra of 1/2metUf, 1/2metUfMoO_4, and 1/2metUfPO_4 from 12 000 to 34 000 cm^{-1}. 1/2metUf shows two broad positive peaks at ~19 000 and ~31 500 cm^{-1} in Abs, at ~20 000 and ~28 800 cm^{-1} in the CD, and at ~18 500 and ~29 000 cm^{-1} in the MCD spectrum. The MoO_4^{2-}-bound form contributes two positive peaks in the CD spectrum at ~20 000 and ~28 500 cm^{-1}, and at ~19 000 and ~28 500 cm^{-1} in the MCD spectrum. The Abs spectrum shows one obvious peak at ~18 500 cm^{-1} and a shoulder at ~30 000 cm^{-1}. The PO_4^{3-} derivative has one peak at ~20 000 cm^{-1} and a shoulder at about 29 000 cm^{-1} in the Abs spectrum. The CD spectrum shows positive transitions at ~20 000 and ~28 500 cm^{-1}, and the MCD spectrum shows bands at ~17 500 and ~29 000 cm^{-1} with additional positive intensity to higher energy. The two features observed in ~20 000 and ~30 000 cm^{-1} in the Abs, CD, and MCD spectra of all derivatives are assigned as tyrosinate to ferric charge transfer transitions from resonance Raman spectroscopy.[28,35,47]

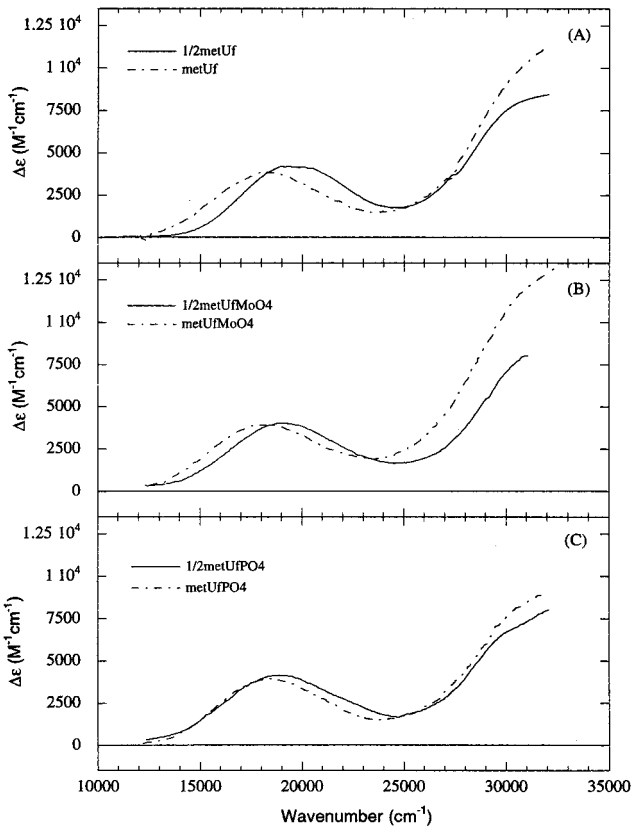

Figure 3. CD spectra of 1/2met (—) and met (-·-) forms in the charge transfer region: (A) uteroferrin, (B) MoO_4 bound uteroferrin, and (C) PO_4 bound uteroferrin. The CD spectra were recorded at 5 °C

The Abs spectra of the fully-oxidized met form of all three derivatives are given in Figure 3 and compared to the analogous 1/2met features. Oxidation to the $Fe^{III}Fe^{III}$ met form results in a shift to lower energy of the Abs bands. The lower energy transition shifts from ~19 700 cm^{-1} to about 18 000 cm^{-1}, and its intensity decreases. The shift of the higher energy transition is less obvious, but the intensity of this transition significantly increases upon oxidation.

Simultaneous Gaussian resolution[65] of the Abs, CD, and MCD spectra of the three 1/2met forms (Figure 4) indicates that at least three bands are required to fit the transition in the ~20 000 cm^{-1} region, while the ~30 000 cm^{-1} region requires at least two bands. A summary of the Gaussian fitting results for 1/2metUf and its derivatives is given in Table 1.

Figure 5 presents a reasonable energy level diagram for the phenolate to Fe^{III} charge transfer transitions. For a ferric ion in an octahedral coordination environment, the five d orbitals split into e_g and t_{2g} sets. They are further split in energy due to a strong interaction along the *z*-axis, which is defined as the direction along the strong Fe−O−Tyr bond. The d_{z^2} and $d_{x^2-y^2}$ are mainly σ bonding orbitals while d_{xz}, d_{yz}, and d_{xy} have mostly π character. The phenolate−Fe bond involves donor interaction of two oxygen p-orbitals perpendicular to the C−O axis, which are the out-of-plane π_{op} and the in-plane π_{ip} orbitals. The 2p orbital along the C−O axis is strongly involved in σ bonding to the carbon atom and is at much deeper binding energy. The energies of the two π orbitals in the phenolate are different due to their degree of conjugation into the ring: π_{op} is perpendicular to the plane and at higher energy than π_{ip}. X-ray crystallographic data on the $Fe^{III}-Zn^{II}$ kidney bean purple acid phosphatase[23,24] indicate that the phenolate binds to the ferric ion with an angle of 136°, and the Fe−O−C plane has a dihedral angle of 39° relative to the plane of the phenolate ring (Figure 4A). In this orientation, d_{z^2} overlaps both the π_{op} and π_{ip}

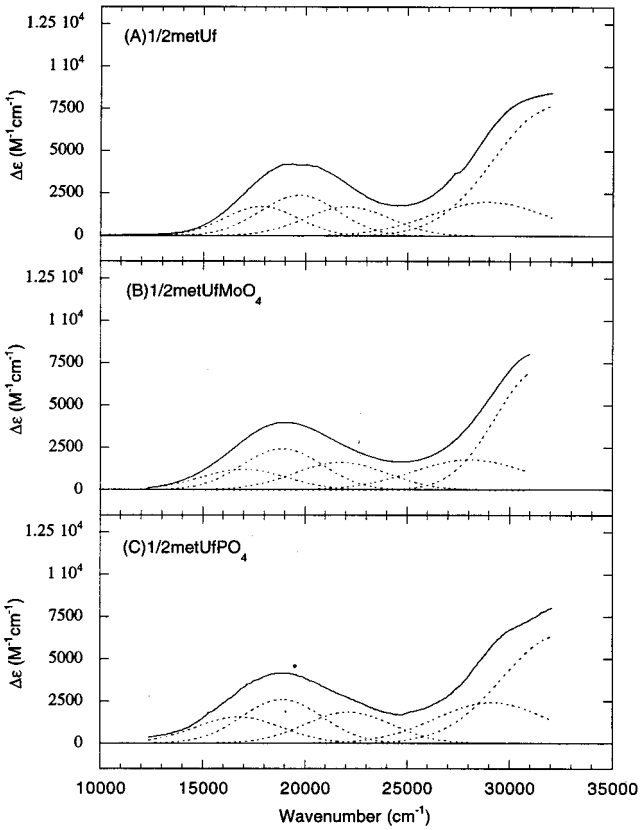

Figure 4. Gaussian resolution of (A) 1/2metUf, (B) 1/2metUfMoO_4, and (C) 1/2metUfPO_4 observed in the charge-transfer room temperature absorption spectra. The experimental spectra (—) were fit to individual Gaussian band shapes (- - -).

orbitals. This also occurs for the d_{xz} and d_{yz} orbitals. The $\pi_{ip} \rightarrow d_{z^2}$ and $\pi_{op} \rightarrow d_{z^2}$ transitions should be at highest energy. These transitions involve mainly σ orbital overlap; thus, they should have the highest charge transfer Abs intensity. The band at ~32 000 cm^{-1} is then assigned as the $\pi_{ip} \rightarrow d_{z^2}$ transition and the band at ~29 000 cm^{-1} is assigned as the $\pi_{op} \rightarrow d_{z^2}$ transition. Their energy difference indicates that the energy splitting between the two π orbitals of the phenolate ligand is about 3000 cm^{-1} (Figure 4B). The $\pi_{ip} \rightarrow d_{xz}$, $\pi_{ip} \rightarrow d_{yz}$, $\pi_{op} \rightarrow d_{xz}$, and $\pi_{op} \rightarrow d_{yz}$ transitions should all contribute in the lower energy charge transfer region with reduced intensity because they involve mainly π orbital overlap. The minimum of three bands required to fit the ~20 000 cm^{-1} region in Figure 3 should correspond to these four charge transfer transitions. The value of the 10Dq of the Fe(III) site can then be estimated from the σ/π splitting of the charge transfer spectrum at ~11 000 cm^{-1}.

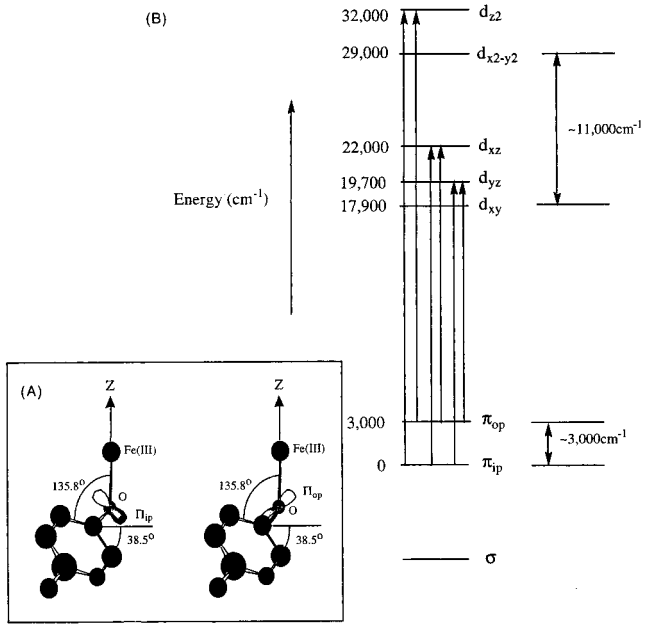

Figure 5. (A) The orbital orientation of the phenolate−ferric bonding. (B) Energy level diagram of the phenolate to ferric charge transfer transitions.

From Figure 3, a red shift occurs in the charge transfer Abs spectra when 1/2metUf and its derivatives are oxidized to the $Fe^{III}Fe^{III}$ met forms. Oxidation of the ferrous ion should shift the electron density of the μ-OH bridge toward this center, thus reducing the bonding interaction of the phenolate bound iron to the μ-OH bridging ligand. The reduced bonding interaction would increase the effective nuclear charge of the phenolate bound ferric center, causing a decrease of the energies of the d-orbitals, thus red shifting the charge transfer transitions. Furthermore, the reduced bonding interaction of the μ-OH to the phenolate bound ferric center should also increase the strength of the Tyr−Fe^{III} bond, which increases the σ overlap and charge transfer intensity at ~30 000 cm^{-1}. Addition of MoO_4^{2-} and PO_4^{3-} causes the transitions at ~20 000 cm^{-1} to decrease in energy (Figure 4), which indicates that the energy of d orbitals on the ferric center decreases. Thus, both MoO_4^{2-} and PO_4^{3-} binding perturb the Fe^{III} center. However, phosphate binding results in a more significant red-shift of the ~20 000 cm^{-1} transition than does molybdate binding ($\Delta E(MoO_4^{2-})$ = ~350 cm^{-1}, $\Delta E(PO_4^{2-})$ = ~760 cm^{-1}), indicating that phosphate binding causes an increase in the donor interaction of the Tyr with the Fe^{III} center. The general similarity of the spectra among three forms suggests that the geometric structure of the ferric site does not significantly change upon anion binding and that there is no change in the bound phenolate or the μ-OH

Table 1. Summary of Abs, CD, and MCD Gaussian Resolution for 1/2met, 1/2metUfMoO_4, and 1/2metUfPO_4 in the Charge Transfer Region

		1/2metUf			1/2metUfMoO_4			1/2metUfPO_4		
band		Abs	CD	MCD	Abs	CD	MCD	Abs	CD	MCD
1	energy (cm^{-1})	17900	18000	18100	17000	17200	17300	16800	17300	17000
	hwhm (cm^{-1})[a]	2400	2000	1800	2200	1300	1300	2500	2200	2000
2	energy (cm^{-1})	19700	20000	20000	18900	19100	19200	18900	19000	19000
	hwhm (cm^{-1})	2100	2000	1800	2300	1800	1300	2300	2000	1800
3	energy (cm^{-1})	22100	22300		21800	21800	22000	22100	22600	22400
	hwhm (cm^{-1})	2200	1800		2300	2000	1500	1800	1400	1400
4[b]	energy (cm^{-1})	28900	28800	28600	28000	28500	28200	29200	28800	29100
	hwhm (cm^{-1})	2500	1500	1300	2500	1200	1200	1500	1300	1300
5[b]	energy (cm^{-1})	32000		31800	3500		31800	32500		
	hwhm (cm^{-1})	2500		1300	2500		1300	1500		

[a] hwhm = half width at half-maximum height. [b] Bands of the Abs are on the shoulder region. Thus the band widths are not able to be well-resolved.

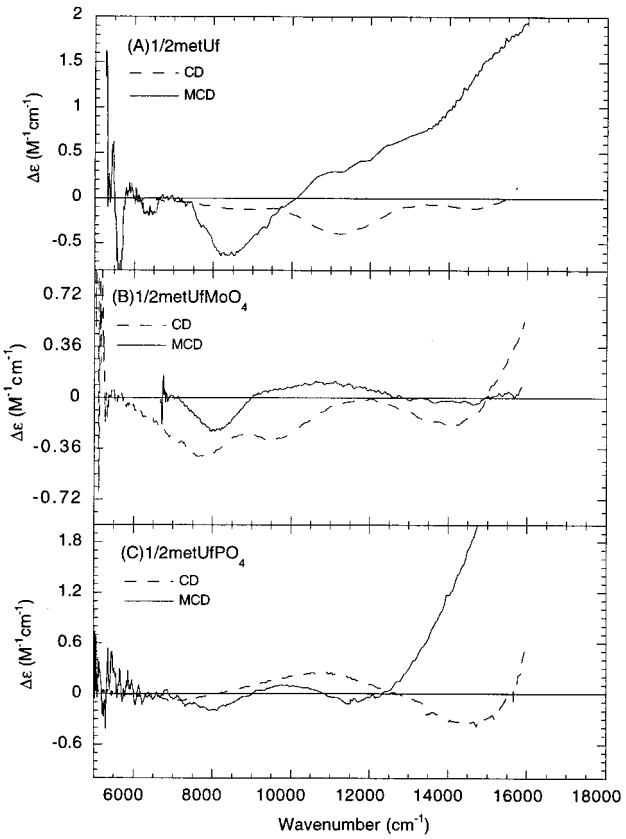

Figure 6. CD (- - -) and LT MCD (—) spectra of the binuclear non-heme $Fe^{II}Fe^{III}$ active site of uteroferrin in the ligand field region: (A) 1/2metUf, (B) 1/2metUfMoO_4, and (C) 1/2metUfPO_4. The CD and low-temperature MCD spectra were recorded at 5 °C and 5K/7T, respectively.

bridge. Thus both MoO_4^{2-} and PO_4^{3-} appear to bind to the ferric site with replacement of an exchangable ligand in the equatorial plane, and phosphate has a strong perturbation to the Tyr → Fe^{III} bond.

B. Ligand Field Transition Region. The CD and MCD spectra of 1/2metUf, 1/2metUfMoO_4, and 1/2metUfPO_4 in the 5000 to 16000 cm^{-1} region are shown in Figure 6. The CD spectrum of 1/2metUf has three negative peaks at ∼8500, 11500, and 14500 cm^{-1}. The ligand field MCD spectrum shows one negative peak at ∼8500 cm^{-1} and a broad positive shoulder above ∼10000 cm^{-1}. The CD spectrum of 1/2metUfMoO_4 has three negative peaks at ∼7500, 9500, and 14000 cm^{-1}. Its MCD spectrum shows two negative peaks at ∼8000 cm^{-1} and ∼14000 cm^{-1}, and a broad positive peak at ∼10800 cm^{-1}. 1/2metUfPO_4 shows two negative peaks in its CD spectrum at ∼7500 and 14500 cm^{-1} and a positive intense peak at ∼11000 cm^{-1}. Two negative peaks at ∼8000 and ∼12000 cm^{-1} and another positive band at ∼10000 cm^{-1} are observed in its MCD spectrum.

Oxidation of the three 1/2met derivatives to the purple met derivatives results in a broad low-energy negative band in their CD spectra. From Figure 7 all met derivatives show one obvious peak and a shoulder in the region of ∼11 000 to ∼15 000 cm^{-1}. Gaussian analysis in Figure 7B indicates that there are two bands required to fit all the metUf CD spectra, which are at ∼12 000 and 13 500 cm^{-1}.

Ferrous and ferric ligand field (d−d) transitions are observed in this region. As summarized in Figure 8, four bands are required to simultaneously fit the CD and MCD spectra of each of the three derivatives. Since oxidation to the met derivatives (Figure 7) eliminates the two bands below 11 000 cm^{-1}, these can be assigned as ferrous d → d transitions**.** The two transitions

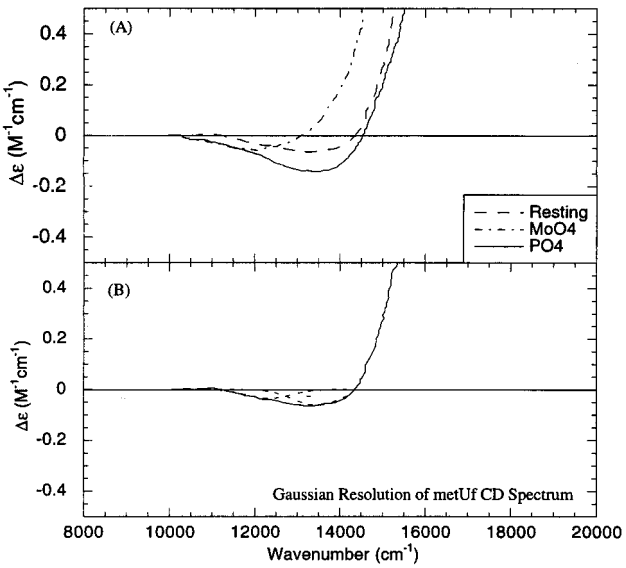

Figure 7. (A) CD spectra of metUf (- - -), metUfMoO_4 (-·-) and metUfPO_4 (—) in the ligand field region. Data were collected at 5 °C. (B) Gaussian resolution of metUf observed in the ligand field CD spectrum. The experimental spectra (—) were fit to individual Gaussian band shapes (- - -).

in the >11 000 cm^{-1} region which are still present in the met derivatives are ferric d → d transitions. The ligand field transitions are summarized in Table 2. The two ferrous d → d transitions observed for all three 1/2met derivatives in the MCD spectrum are in the range of ∼10 000 cm^{-1} and split by ∼2000 cm^{-1}, which indicates that the ferrous center is six-coordinate. It is apparent that both anions perturb the ferrous site. The ligand field spectrum indicates that the Fe^{II} remains six coordinate after anion binding, implying that both anions replace one ligand (likely water) at the ferrous site. The two ferrous d → d transitions decrease in energy with the MoO_4^{2-} and PO_4^{3-} binding, indicating that 10Dq has decreased. The ligand field strength of the ferrous center follows the order 1/2metUf > 1/2metUfMoO_4 > 1/2metUfPO_4.

All d−d transitions of high-spin ferric sites are spin-forbidden and therefore have very low extinction coefficients and in most cases are not detectable by absorption spectroscopy in proteins. However, these transitions can gain intensity from mixing with the low-energy intense phenolate to Fe^{III} charge transfer transitions. The energies of these d−d transitions are sensitive to the geometry and bonding interactions of the ferric site and can also be used to probe this center.

From LF theory, the lowest energy d−d transitions for a high-spin ferric site with cubic symmetry are the $^6A_1 \rightarrow {}^4T_1$ and $^6A_1 \rightarrow {}^4T_2$, with the $^6A_1 \rightarrow {}^4T_1$ transition at lower energy. Typically, these are the only ferric bands in the near-IR region. Thus, the two ferric d → d transitions of the three 1/2met species in the region between ∼11 000 and ∼15 000 cm^{-1} (Figure 8) can be assigned as the $^6A_1 \rightarrow {}^4T_1$ and $^6A_1 \rightarrow {}^4T_2$ transitions. The energy of $^4T_1$ is observed to decrease upon anion binding. This transition involves exciting an electron from the antibonding e_g orbital to the lower energy, half-filled t_{2g} level ($t_{2g}^3e^2 \rightarrow t_{2g}^4e_g^1$), thus a stronger ligand field results in a lower energy transition. The ferric $^4T_2$ d−d transition also decreases in energy upon the anion binding. The energies of these transitions (∼12 600 and ∼15 000 cm^{-1}) indicate that the ferric site of Uf is six coordinate, based on non-heme ferric model complex data *(vide supra)*. The coordination number does not change upon anion binding, indicating that the anions likely perturb the ferric center by replacing a solvent ligand. Furthermore, the decrease

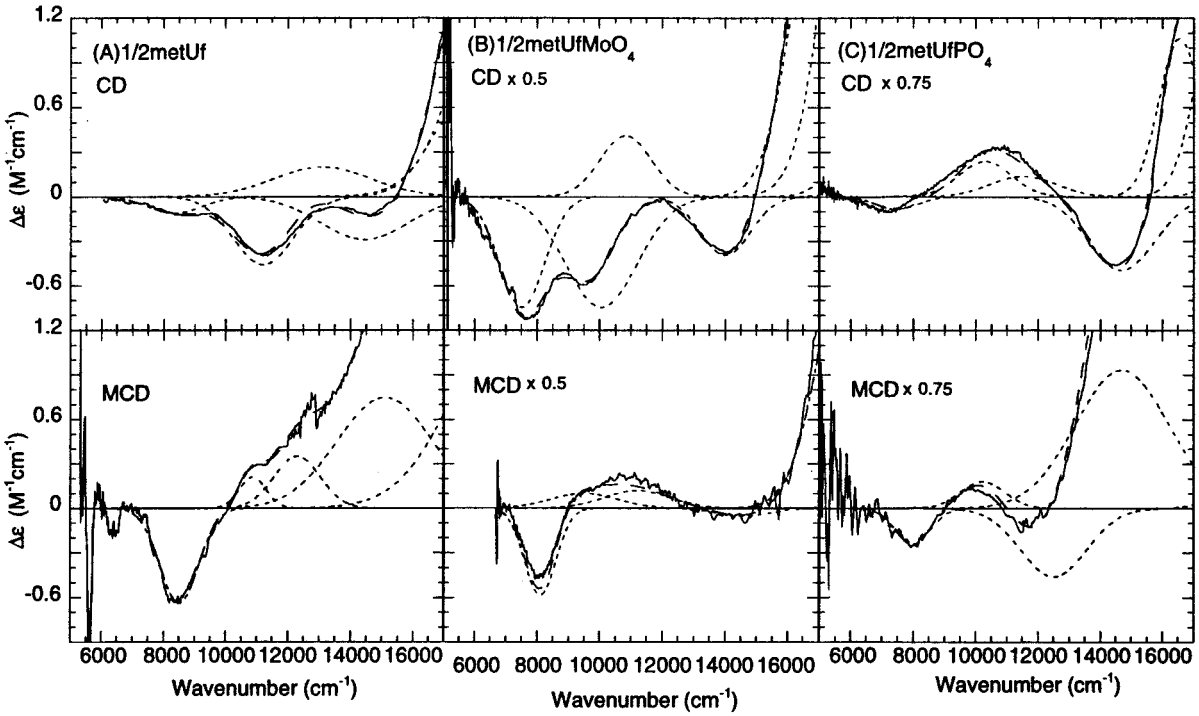

Figure 8. Gaussian resolution of (A) 1/2metUf, (B) 1/2metUfMoO_4, and (C) 1/2metUfPO_4 observed in the ligand field CD (top) and MCD (bottom) spectra. The experimental spectra (—) were fit to individual Gaussian band shapes (- - -).

Table 2. Summary of CD and MCD Gaussian Fitting Results for 1/2metUf, 1/2metUfMoO_4, and 1/2metUfPO_4 in the Ligand Field Region

		1/2metUf		1/2metUfMoO_4		1/2metUfPO_4	
band		CD	MCD	CD	MCD	CD	MCD
1	energy (cm^{-1})	8500(−)	8500(−)	7600(−)	7900(−)	7600(−)	7900(−)
Fe^{2+}, d−d(x^2-y^2)	hwhm (cm^{-1})	1000	800	900	600	800	700
2	energy (cm^{-1})	11200(−)	11000(+)	10000(−)	9800(+)	10300(+)	10100(+)
Fe^{2+}, d−d(z^2)	hwhm (cm^{-1})	1100	800	1200	900	1000	800
3	energy (cm^{-1})	12900(+)	12600(+)	11000(+)	11200(+)	11800(+)	12200(−)
Fe^{3+}, $^6A_1 \rightarrow {}^4T_1$	hwhm (cm^{-1})	1500	1100	1100	1000	1200	1200
4	energy (cm^{-1})	14800(−)	15000(+)	14000(−)	14300(−)	14600(−)	14700(+)
Fe^{3+}, $^6A_1 \rightarrow {}^4T_2$	hwhm (cm^{-1})	1700	1500	1300	1300	1700	1400

in transition energy upon the anion binding indicates that the anions have stronger ligand field compared to the replaced ligand.

The changes observed in both the CD and MCD spectra in the ligand field region for all three derivatives demonstrate that MoO_4^{2-} and PO_4^{3-} perturb both the ferrous and ferric sites, indicating that they bind to the active site in a bridging mode. The ligands replaced are likely water or hydroxide derived solvent ligands. Under the acidic conditions used in this study (pH = 4.5−5.5), which corresponds to high enzymatic activity, the solvent-derived ligand of the ferric site should be deprotonated, while the ferrous site should have a bound water. The fact that the ferric d → d transitions decrease in energy indicates that anion binding increases their 10Dq value, reflecting the fact that the oxo anion is a stronger field ligand than OH^-. Additionally, anions decrease the 10Dq of the ferrous site consistent with the fact that they replace H_2O, which has a higher ligand field strength. These results indicate that MoO_4^{2-} and PO_4^{3-} should have ligand field strengths between hydroxide and water, which is reasonable based on the spectrochemical series considering these to be similar to oxalate.

C. Ground State. The intensity for 1/2metUf, 1/2metUf-MoO_4, and 1/2metUfPO_4 increases as the temperature decreases, indicating that these transitions are MCD *C*-terms, associated with paramagnetic doublet ground states which are split in energy by the magnetic field. The variable-temperature variable-field MCD intensities measured for the positive bands at ~20 000 cm^{-1} are given in Figure 9 (symbols, with the standard deviation shown as an error bar for each datum point). The variable-field saturation curves obtained at fixed increasing temperatures when plotted as a function of $\beta H/2kT$ do not superimpose, but are nested, which is associated with the population of higher excited states. Comparison of the saturation curves of the three derivatives reveals that they have different saturation behavior. In particular, the phosphate-bound form is very different from the resting and molybdate-bound forms, indicating that the energies of the higher excited states are different.

The VTVH data were fit by using the MCD intensity expression for a Kramers system, which allows for the effects of a linear *B*-term (from field-induced mixing with higher energy states) and the presence of excited states, eq 2:[66−68]

$$\Delta\epsilon = \sum_i (A_{\text{satlim}})_i \left[\int_0^{\pi/2} \frac{\cos^2\theta \sin\theta}{\Gamma_i} g_{\parallel i} \alpha_i \, d\theta - \sqrt{2}\frac{M_z}{M_{x,y}} \int_0^{\pi/2} \frac{\sin^3\theta}{\Gamma_i} g_{\perp i} \alpha_i \, d\theta \right] + \sum_i B_i \gamma_i H \quad (2)$$

where

Table 3. VTVH MCD Parameters for the Ground State and Lowest Excited States of 1/2metUf, 1/2metUfMoO$_4$, and 1/2metUfPO$_4$

	VTVH MCD											
	GS						ES					
	A_{sat}	B (% of A_{sat})	$g_{\|\|}$	$g_{\perp}$	E (cm^{-1})	$M_z/M_{x,y}$	A_{sat}	B (% of A_{sat})	$g_{\|\|}$	$g_{\perp}$	E (cm^{-1})	$M_z/M_{x,y}$
1/2metUf	7.55	0.5723	1.94	1.65	0.00	0.29	2.31	1.0583	6.00	0.00	12.62	0.29
1/2metUfMoO$_4$	7.85	0.4851	1.97	1.52	0.00	0.28	4.03	0.8296	6.00	0.00	18.37	0.28
1/2metUfPO$_4$												

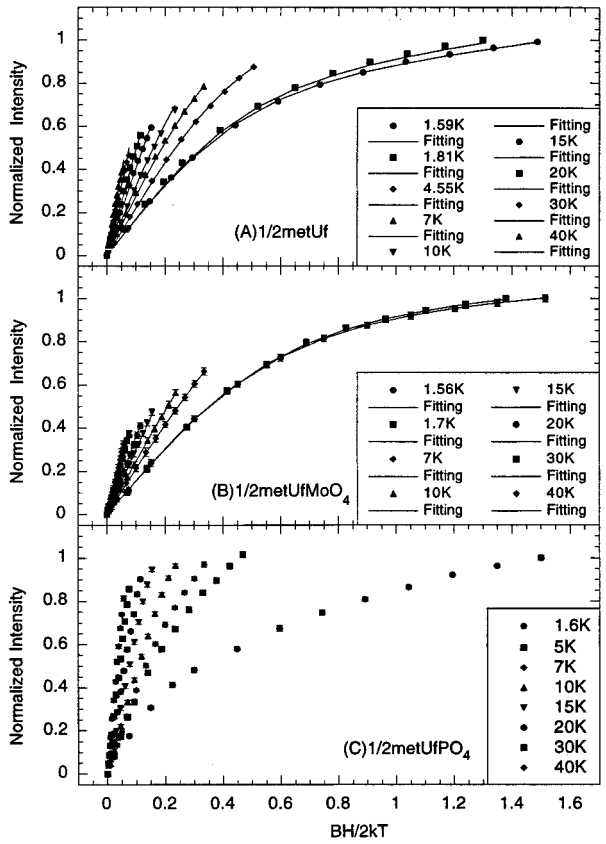

Figure 9. Saturation magnetization behavior of the MCD signal in the charge transfer region for (A) 1/2metUf at 28 168 cm^{-1}, (B) 1/2metUfMoO$_4$ at 28 168 cm^{-1}, and (C) 1/2metUfPO$_4$ at 28 168 cm^{-1}. The intensity amplitude (symbol) for a range of magnetic field (0−7.0 T) at a series of fixed temperatures is plotted as a function of $\beta H/2kT$. The fit to the VTVH MCD data (solid line) of 1/2metUf and 1/2metUfMoO$_4$ was obtained by substituting the parameters shown in Table 3 into eq 2.

$$\Gamma_i = \sqrt{(g_{\|i}\cos\theta)^2 + (g_{\perp i}\sin\theta)^2}$$

$$\alpha_i = \frac{e^{-(E_i-\Gamma_i/2)/kT} - e^{-(E_i+\Gamma_i/2)/kT}}{\sum_j e^{-(E_j-\Gamma_j/2)/kT} + e^{-(E_j+\Gamma_j/2)/kT}}$$

$$\gamma_i = \frac{e^{-(E_i)/kT}}{\sum_j e^{-(E_j)/kT}}$$

$(A_{satlim})_i$, $g_{\|i}$, $g_{\perp i}$, and B_i are the *C*-term MCD intensity, the dimer *g* values, and the *B*-term MCD intensity of the *i*th doublet, respectively. E_i is the energy of the *i*th state, and the energy of the ground state is defined as zero. Boltzmann population over all states has been included for both the *C*-term and the *B*-term intensity with the factors α_i and γ_i. H is the applied magnetic field, and *k* is the Boltzmann constant. M_z and $M_{x,y}$ are the transition dipole moments for the *z*- and *x,y*-polarized directions.

Table 4. 1/*T* MCD Parameters for the Ground State and Lowest Excited States of 1/2metUf, 1/2metUfMoO$_4$, and 1/2metUfPO$_4$

	1/*T* MCD					
	GS			ES		
	A_{sat}	B	E (cm^{-1})	A_{sat}	B	E (cm^{-1})
1/2metUf	21.13	−0.60	0.0	65.28	1.55	22.56
1/2metUfMoO$_4$	14.76	0.43	0.0	35.53	−0.05	18.54
1/2metUfPO$_4$	28.67	−2.88	0.0	76.70	7.83	6.61

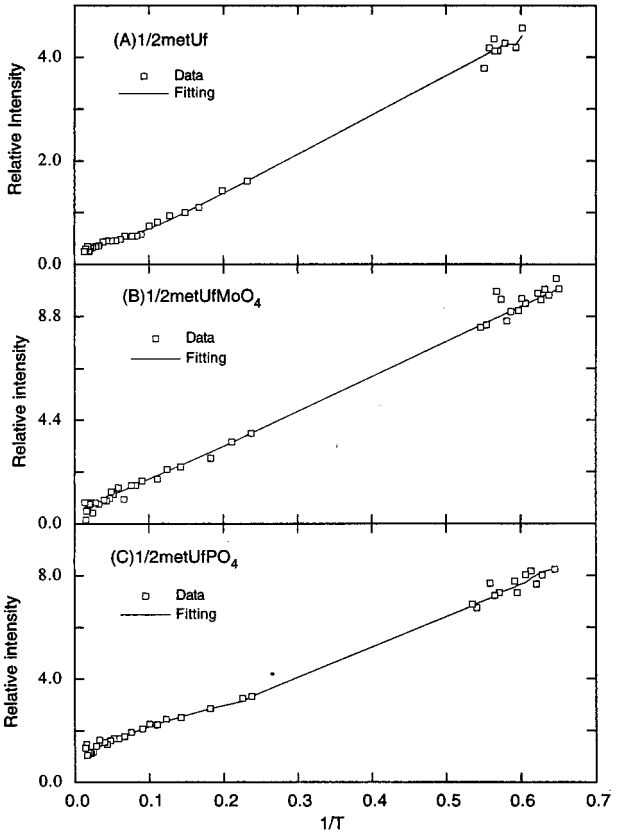

Figure 10. Temperature dependence of the MCD signal in the charge transfer region for (A) 1/2metUf at 28 168 cm^{-1}, (B) 1/2metUfMoO$_4$ at 28 168 cm^{-1}, and (C) 1/2metUfPO$_4$ at 28 168 cm^{-1}. The intensity amplitude (symbol) for a range of temperature (1.5−70 K) at a fixed field of 0.5 T is plotted as a function of 1/*T*. The fit to the 1/*T* MCD data (solid line) was obtained by substituting the parameters shown in Table 4 into eq 3.

The lowest temperature VTVH MCD data for 1/2metUf were fit by using eq 2, allowing the polarization ratio ($M_z/M_{x,y}$), $(A_{satlim})_0$, and B_0 to be adjustable parameters. The ground state dimer *g* values were taken from EPR data. $A_{satlim} = 7.55$, $B =$ 0.57%, and $M_z/M_{x,y} = 0.29$ were obtained. The calculated curves deviate from the data points for the higher temperature isotherms due to the Boltzmann population of the higher sublevels with $E_i \neq 0$. To fit the whole data set, a second doublet (first excited state) was included with the same polarization ratio, but A_{satlim} and *B* were allowed to vary. The best fit to the complete data set is shown in Figure 8A and

Table 5. Spin Hamiltonian Parameters for 1/2metUf, 1/2metUfMoO_4, and 1/2metUfPO_4

	1/2metUf	1/2metUfMoO_4	1/2metUfPO_4
$-J$ (cm^{-1})	$> 5.50 \pm 0.65$	8.12 ± 0.70	3.24 ± 0.20
$D_{Fe^{2+}}$ (cm^{-1})	$+5.17 \pm 0.20$	$+7.76 \pm 0.10$	-9.84 ± 0.60
$E_{Fe^{2+}}/D_{Fe^{2+}}$	0.17 ± 0.02	0.00	0.32 ± 0.02
k^2	0.60 ± 0.02	0.81 ± 0.02	0.79 ± 0.02
$g_{z,Fe^{2+}}$	2.03 ± 0.05	2.05 ± 0.05	2.57 ± 0.05
$g_{y,x-Fe^{2+}}$	2.23 ± 0.05	2.25 ± 0.05	2.24 ± 0.05
$g_{x,y-Fe^{2+}}$	2.17 ± 0.02	2.25 ± 0.02	2.40 ± 0.03
$D_{Fe^{3+}}$ (cm^{-1})	-0.84 ± 0.04	-0.20 ± 0.07	1.13 ± 0.10
1st ex state E	12.65 ± 2.00	18.35 ± 2.00	6.60 ± 0.50

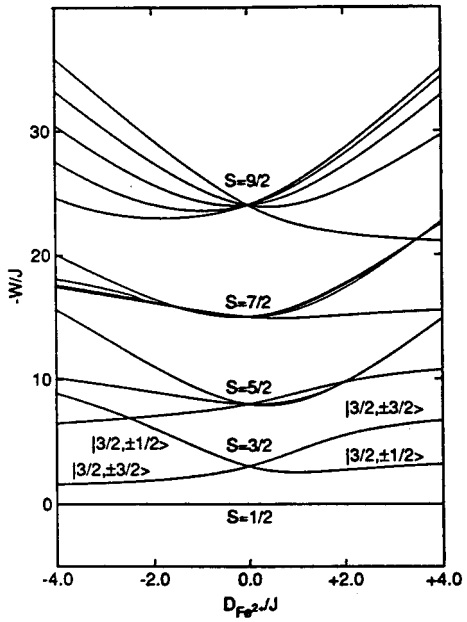

Figure 11. Energy level diagram for a mixed-valence dimer with coupled $S = {}^5/_2$ and $S = 2$ predicted by eq 4. The m_s components of the $S_{tot} = {}^3/_2$ are also included. The energy of the $S_{tot} = {}^1/_2$ state has been set to zero.

Table 3. This fit corresponds to an excited state energy of ~13 cm^{-1}, and A_{satlim} and B equal to 2.31 and 1.05%, respectively. Fits with an excited state energy lower than 10 cm^{-1} were poor (visually and based on a goodness of fit parameter), while for energy above ~13 cm^{-1} the goodness of fit was relatively flat. Thus a lower limit on the excited state energy of $>13 \pm 2$ cm^{-1} is required by the VTVH MCD data for 1/2metUf. The lowest temperature VTVH MCD data of 1/2metUfMoO_4 can also be fit with one doublet with $A_{satlim} = 7.85$, $B = 0.49\%$, and $M_z/M_{x,y} = 0.28$. Higher temperature data deviate from this fit, requiring an excited state doublet with an energy of 18 cm^{-1} for the best fit (Figure 8B and Table 3). The goodness-of-fit parameter significantly increases when the first excited-state energy is raised or lowered, indicating that 18 ± 2 cm^{-1} is a well-defined minimum. Inclusion of a third state for either derivative does not have a significant effect on the fitting results. The similarity of the parameters obtained for 1/2metUf and 1/2metUfMoO_4 indicates that they have a similar $S_{tot} = {}^1/_2$, $M_s = \pm{}^1/_2$ ground state. A good fit could not be obtained for the lowest temperature saturation MCD data of 1/2metUfPO_4 due to the presence of a very low lying excited state (which results in the crossover of sublevels at high magnetic field) as described below.

To avoid the possibility of crossover of sublevels, variable-temperature MCD data were also collected at a fixed low magnetic field of 0.5 T for 1/2metUf, 1/2metUfMoO_4, and 1/2metUfPO_4 (Figure 10, symbols). The intensity versus $1/T$ is not linear in the higher temperature region, which would be expected for an isolated Kramers doublet ground state (Curie law) indicating population of higher states. Deviation results from the population of the low-lying excited state with the increase of the temperature, thus a first excited state ($i = 1$) is required to obtain a reasonable fit for all derivatives.

The MCD intensity can be alternatively expressed in eq 3,[69] where the diamagnetic (*A*- and *B*-term) contributions have been considered as a single constant B_i:

$$\Delta\epsilon = \sum_i \left(\frac{C_i}{kT} + B_i\right)\alpha_i H \qquad (3)$$

where

$$\alpha_i = \frac{e^{-E_i/kT}}{\sum_j e^{-E_j/kT}}$$

$\Delta\epsilon$ is the experimental MCD intensity, C_i ($i = 0, 1, 2, ...$), B_i, and E_i are the MCD *C*- and *B*-term intensity parameters and the energy of the *i*th doublet ($E_0 = 0.0$). Boltzmann population over all states is included as α_i for both the *C*-term and the *B*-term intensities. H is the applied magnetic field, and k is the Boltzmann constant.

$1/T$ data for 1/2metUf and 1/2metUfMoO_4 were fit to eq 3 with C_i, B_i, and E_i as adjustable parameters. 1/2metUf has an excited state with the energy of 23 cm^{-1}. MoO_4 binding changed the first excited state energy to $E = 19$ cm^{-1}. Both fits have shallow minima (i.e., changing E_i does not greatly affect the goodness of fit). The best fits are given in Figure 9 (solid lines) and Table 4.

Thus the MCD data for 1/2metUf can only give a lower limit of ~13 cm^{-1} for its first excited state, while for 1/2metUfMoO_4 the first excited state is at ~18 cm^{-1} from both the VTVH and $1/T$ MCD analyses, which can then be considered as a good estimate. The addition of HPO_4^{2-} dramatically decreases the first excited energy to $E_1 = 6.6 \pm 0.5$ cm^{-1}. Fits with lower or higher energies are very poor on the basis of the goodness-of-fit parameter. The larger *B*-term for 1/2metUfPO_4 is also consistent with the first excited state energy being lower than that for 1/2metUf and 1/2metUfMoO_4. These results indicate that PO_4 binding has a different perturbation on the active center of Uf compared to MoO_4 binding. In order to interpret the excited state energies obtained from VTVH and $1/T$ MCD analyses and the dimer g values obtained from EPR spectra, we consider the ground state for a coupled binuclear $Fe^{II}Fe^{III}$ system. A High-spin ferrous ion has an $S = 2$ ground state with $M_s = 0, \pm1, \pm2$. The high-spin ferric ion has a $^6A_1$ ground state with $S = {}^5/_2$ and $M_s = \pm{}^1/_2, \pm{}^3/_2$, and $\pm{}^5/_2$. The $(2S + 1)$ M_s degeneracy of the ground state of each iron will split in energy due to zero-field splitting. In an exchanged coupled binuclear system, the Fe^{II} $S = 2$ will interact with the Fe^{III} $S = {}^5/_2$ to give five $S_{tot} = |S_1 + S_2|, ..., |S_1 - S_2| = {}^9/_2, {}^7/_2, {}^5/_2, {}^3/_2$, and ${}^1/_2$ levels. These levels are split by the exchange interaction $H = 2JS_1S_2$ to generate $(2S_{tot} + 1)$ M_s degenerate levels at the energies of $3J$, $5J$, $7J$, and $9J$. $S_{tot} = {}^1/_2$ is the ground state when the two irons are antiferromagnetically coupled.

The combined effects of exchange coupling and zero-field splitting in the 1/2met site can be described by the spin Hamiltonian given in eq 4, which operates over the uncoupled basis set $|S_{Fe^{2+}}, S_{Fe^{3+}}, m_{sFe^{2+}}, m_{sFe^{3+}}\rangle$ with the resulting dimer wave functions expressed as $|S_{tot}, \pm M_s\rangle$.

$$H = -2JS_{Fe^2} + S_{Fe^{3+}} + D_{Fe^{2+}}(S^2_{zFe^{2+}} - 2) + E_{Fe^{2+}}(S^2_{xFe^{2+}} - S^2_{yFe^{2+}}) + D_{Fe^{3+}}(S^2_{zFe^{3+}} - 35/12) + g_{zFe^{2+}}\beta H_z S_{zFe^{2+}} + g_{xFe^{2+}}\beta H_x S_{xFe^{2+}} + g_{yFe^{2+}}\beta H_y S_{yFe^{2+}} + g_{zFe^{3+}}\beta H_z S_{zFe^{3+}} + g_{xFe^{3+}}\beta H_x S_{xFe^{3+}} + g_{yFe^{3+}}\beta H_y S_{yFe^{3+}} \quad (4)$$

with

$$D_{Fe^{2+}} = (-k^2\lambda_0/4)(g_{xFe^{2+}} + g_{yFe^{2+}} - 2g_{zFe^{2+}}) \quad (5a)$$

$$E_{Fe^{2+}} = (-k^2\lambda_0/4)(g_{yFe^{2+}} - g_{xFe^{2+}}) \quad (5b)$$

Included in eq 4 are the exchange coupling constant J, the axial ($D_{Fe^{2+}}$, $D_{Fe^{3+}}$) and rhombic ($E_{Fe^{2+}}$) zero field splitting (ZFS), and the Zeeman effect ($g_{zFe^{2+}}\beta H_z S_{zFe^{2+}}$, etc.). The single site g_i value for a Fe^{II} can be related to the ZFS parameters by using ligand field theory as given in eqs 5a and 5b, where λ_0 is the Fe^{2+} ground state spin−orbit coupling constant (∼100 cm^{-1}) and k^2 is the Stevens orbital reduction factor, which is <1 due to convalency.

Application of eq 4 results in a 30 × 30 matrix. Diagonalization of this matrix in zero magnetic field with $D_{Fe^{3+}} = E_{Fe^{2+}} = 0$ cm^{-1} gives the energy level diagram in Figure 11, where the energy (W) is given in the reduced energy parameter W/J as a function of $D_{Fe^{2+}}/J$. Note the ZFS splitting of the $S_{tot} = {}^3/_2$ first excited spin state of the dimer, as the VTVH MCD data are most sensitive to this substate. For positive $D_{Fe^{2+}}/J$, the $|{}^3/_2, \pm{}^1/_2\rangle$ state is lowest in energy, while for negative $D_{Fe^{2+}}/J$, the $|{}^3/_2, \pm{}^3/_2\rangle$ is the first excited state. Table 5 gives the values of the ZFS of each iron and the J value of the dimer obtained by applying eq 4 to the experimentally detected first excited state energy (from the VTVH MCD), and the dimer g values (from EPR). J, $g_{yFe^{2+}}$, $g_{zFe^{2+}}$, and $E_{Fe^{2+}}$ were adjustable parameters; $g_{xFe^{2+}}$ and $D_{Fe^{2+}}$ were determined by using eq 5. Depending on the sign of $D_{Fe^{2+}}$, either $g_{yFe^{2+}}$ or $g_{zFe^{2+}}$ was initially held equal to 2.00, but allowed to float in later refinements. The magnitude of $D_{Fe^{2+}}$ was constrained to be less than ∼|15| cm^{-1}, the maximum observed value for Fe^{2+}, and E/D is $\leq {}^1/_3$. The orbital reduction factor on the Fe^{2+} was initially set to 0.80, but was allowed to vary in the final fits. The $g_{Fe^{3+}}$ values were set equal to 2.00, and $D_{Fe^{3+}}$ was an adjustable parameter constrained to be less than ∼1 cm^{-1}. The error ranges given in Table 5 were obtained via floating the first excited state energy within the range obtained from the VTVH MCD data analysis *(vide supra)*.

The first excited-state energy of >13 cm^{-1} was used for 1/2metUf to obtain a lower limit estimate of its exchange coupling constant. This gives a $-J$ value of >6 cm^{-1}, which is in the range of that expected for a μ-OH bridge. MoO_4^{2-} binding results in a J value of ∼−8 cm^{-1}, implying that there is at most a limited perturbation of the μ-OH bridge upon MoO_4^{2-} binding. The ZFS of the Fe^{II} becomes axial in 1/2metUfMoO4; thus, its negative J/D value gives the $|{}^3/_2, \pm{}^3/_2\rangle$ level in the left side of Figure 11 as the first excited state. Alternatively, PO_4^{3-}-bound Uf has a rhombic Fe(II) site. The exchange coupling constant of 1/2metUfPO_4 decreases to −3 cm^{-1}, implying that there is a large effect of the PO_4^{3-} on the μ-OH bridging ligand. The low J value indicates that the first excited state of 1/2metUfPO_4 is at low energy. At a field of 4 T this will become thermally populated under low-temperature conditions and affect the saturation magnetization curves *(vide supra,* Figure 3*)*. The above results indicate that bound PO_4^{3-} perturbs the ferrous site and the μ-OH bridge in a different manner compared to bound MoO_4^{2-}. The fact that the molybdate bound Uf has an axial Fe^{II} center indicates that the bonding interaction with the μ-OH bridge is weaker, while a more rhombic Fe^{II} site after the phosphate binding implies that there is a stronger bonding interaction between the μ-OH bridge and the Fe^{II} center.

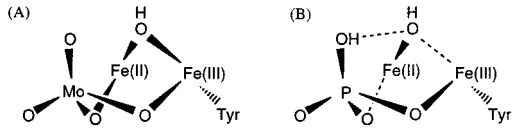

Figure 12. Possible structures of oxo anion binding to the binuclear non-heme $Fe^{II}Fe^{III}$ active site of uteroferrin: (A) molybdate bound 1/2metUf and (B) phosphate bound 1/2metUf. The dashed line in part B indicates a weakened bonding interaction.

Discussion

CD and MCD spectra in the ligand field region for 1/2metUf show two ferrous d−d transitions at ∼10 000 cm^{-1}, split by an energy of ∼2000 cm^{-1}, which indicates that the ferrous center is six-coordinate. Two additional peaks in the near-IR region are identified as ferric d−d transitions. On the basis of model studies the energies of these transitions indicate that the ferric center is also six-coordinate. From the VTVH MCD study of the ground state of 1/2metUf, the exchange coupling constant is $-J > 5.5$ cm^{-1}, indicating the existence of an hydroxo bridging ligand between the iron sites. Compared to BSPAP and KBPAP,[34−38] the J values of all three species are in a range consistent with the presence of a hydroxo bridge. The existence of a hydroxo bridge between two metals and one water derived ligand on each metal resulting in six-coordination has been proposed but not observed in the crystal structure of the Fe^{III}-Zn^{II} form of the enzyme (*vide infra*, Figure 1).

From CD and MCD spectra in the d−d region both the ferrous and ferric centers are perturbed upon the molybdate and the phosphate binding but remain six-coordinate. This implies that exchangable water derived ligands are replaced upon oxoanion binding and that these anions bind to the active center in a bridging mode, which is consistent with the structural studies.[27,45,46,59] Anion binding decreases the 10Dq value of the ferrous site, whereas the 10Dq of the ferric site increases, indicating that the ligand field strengths of the oxoanion ligands are between those of the two replaced ligands. This further supports the presence of a hydroxide ligand on the ferric center and a water ligand on the ferrous site.

Structures for anion binding to 1/2metUf are given in Figure 12, in which the active site has the endogenous tyrosinate ligand bound to the Fe^{III} trans to the μ-OH bridging ligand. Molybdate has pK_{a1} and $pK_{a2} < 3.7$. Thus it is deprotonated under reaction conditions (pH ∼ 4.9). From kinetic studies MoO_4^{2-} first binds to the Fe^{II} replacing the terminal water ligand. It then binds to the Fe^{III} center to form a bidentate bridging ligand with release of the terminal hydroxide. Phosphate binds to the active site in a similar manner. It exists in solution as $H_2PO_4^-$ under the optimal pH of this system and bridges the active site in a bidentate modelikely as HPO_4^{2-}, which has been concluded in kinetic studies.[22]

VTVH and 1/T MCD data show that 1/2metUf has a first excited state located at >13 cm^{-1}. MoO_4^{2-} binding does not significantly change the first excited state energy, indicating that the μ-OH bridge is not significantly perturbed. However, the first excited state energy and the exchange coupling constant J show a significant decrease upon phosphate binding, implying that the μ-OH bridge has been affected by the bound phosphate. Moreover, the Tyr → Fe^{III} charge transfer transition is strongly

red-shifted in the phosphate-bound form, which indicates that the bonding interaction between the Fe^{III} and the μ-OH bridge is weakened and compensated by the Tyr donor. The more rhombic ferrous site further supports a stronger μ-OH−Fe^{II} bond. Alternatively, molybdate binding does not cause a red-shift (*vide supra*, Figure 3); its axial Fe^{II} site also suggests that the μ-OH−Fe^{II} bond is weaker than in the resting enzyme.

The pK_a of HPO_4^{2-} is ∼12.7, which will decrease by several log units upon binding to the iron site due to the inductive effect. David and Que have proposed that H-bonding of the phosphate proton to the μ-OH bridge could occur and be responsible for the reduction in exchange coupling.[56] Other oxoanions when bound in a protonated form have similar spectral effects to those observed with HPO_4^{2-} binding.[56,70] The reduction in J in 1/2metUfHPO_4^{2-} causes a broadening of the EPR spectrum due to large anisotropy in g values.[36] This behavior has also been observed with arsenate ($HAsO_4^{2-}$ at pH ∼4.9)[56] and pyrophosphate ($H_2P_2O_7^{2-}$ at pH ∼4.9) binding.[51] For 1/2metAsO_4, D_2O has been found to change the g values, which has been interpreted as resulting from a change in H-bonding.[56] Formation of a H-bond of the oxoanion to the μ-OH bridge would reduce μ-OH donor interaction with the irons and decrease the exchange coupling constant.

The phenolate ligand plays an important role in this system. It is the strongest donor ligand at the active site. It decreases the redox potential of Fe^{III}/Fe^{II} and stabilizes the mixed-valence state which is active in catalysis. Secondly, it donates significant electron density to the Fe^{III}, which should reduce the donor interaction of the terminal hydroxide to the Fe^{III} and increase the nucleophilicity of the terminal hydroxide, which is considered to be the initiator in the nucleophilic attack on the phosphate ester in the hydrolysis reaction. Moreover, the strong bonding interaction between the phenolate and the Fe^{III} would stabilize the Fe^{III} if the electron donor interaction of the μ-OH bridge is reduced due to a H-bonding interaction with the phosphate.

Phosphate, pyrophosphate, and arsenate binding also induce the oxidation of the active site to the $Fe^{III}Fe^{III}$ level while molybdate stabilizes the $Fe^{II}Fe^{III}$ active state from oxidation.[51] The addition of phosphate and arsenate decreases the reduction potential of the active site while molybdate increases its potential.[57] Phosphate and arsenate are known to have a much higher affinity for the ferric ion than the ferrous ion.[71,72] Thus, in the phosphate- or arsenate-bound forms, there is a stronger electron donor interaction with the ferric ion, which should also contribute to the decrease in the bonding interaction between the ferric ion and the μ-OH bridge. Alternatively, molybdate has a similar affinity for ferric and ferrous ions[71,72] and should not generate as strong an effect on the exchange coupling interaction. Thus both the formation of a hydrogen bond to the μ-OH bridge and a stronger donor interaction of the oxoanion to the Fe^{III} would contribute to the lower J value for 1/2metUfHPO_4.

A reasonable mechanism shown in Scheme 1 for the phosphate ester hydrolysis reaction has been proposed.[22,59,73,74] The oxygen atom from the phosphate ester binds to the active site, replacing the water ligand on the ferrous center. The

Scheme 1

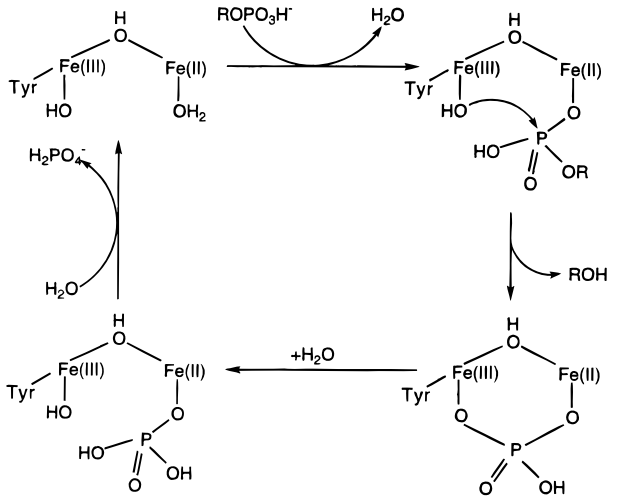

substrate is thus configured such that the terminal hydroxide ligand on the Fe^{III} is capable of nucleophilic attack at the phosphorus center with inversion of configuration.[75,76]

Another pathway for the nucleophilic attack can also occur if the phosphate ester binds to the active site in a similar mode to the phosphate inhibitor. It is possible that the μ-OH bridge can be activated for nucleophilic attack.[46] The decrease of the exchange coupling upon phosphate binding indicates a weakening of the μ-OH bridging ligand. The red-shift of the Tyr−Fe^{III} charge transfer transition also demonstrates that the bonding interaction between the Fe^{III} and the μ-OH bridge is decreased. Thus, phosphate or substrate binding would labilize the μ-OH bridge for nucleophilic attack. It would be important to have isotope labeling studies which distinguish between the μ-OH bridge and the terminal hydroxide on the Fe^{III} in the nucleophilic attack mechanism.

In summary, the spectroscopic methodology applied in this study has provided important insight into the binuclear iron active site of $Fe^{III}Fe^{II}$ uteroferrin and its oxoanion derivatives. Abs, CD, and MCD studies in the charge transfer transition region have derived an energy level diagram of the Tyr−Fe^{III} bond and the effects on this bond of oxoanion binding and on oxidation to the met level. CD and MCD studies in the ligand field region have shown that both Fe^{III} and Fe^{II} are six-coordinate, and remain six-coordinate upon the oxoanion binding. Phosphate binding increases the bonding strength between the μ-OH bridge and the Fe^{II}, causing a more rhombic ferrous center. It further decreases the antiferromagnetic exchange coupling and weakens the bridging interaction of the μ-OH bridge with the Fe^{III}. In addition to structural information which complements with the results of X-ray crystallography, insight into possible electronic structure contribution to reactivity has also been obtained in this study.

Acknowledgment. This work was support by NSF-Biophysics Program Grant No. MCB 9316768.

JA971896J

(71) Sillén, L. G.; Martell, A. E. In *Stability Constants of Metal Ion Complexes*, 2nd ed.; The Chemical Society: London: 1964; Section 2; 1971, Supplement No. 1, Part 2.

(72) Smith, R. M.; Martell, A. E. In *Critical Stability Constants;* Plenum Press: New York, 1989; Vol. 6 and Supplement No. 2.

(73) Aquino, M. A. S.; Lim, J.-S.; Sykes, A. G. *J. Chem. Soc., Dalton Trans.* **1992**, 2135−2136.

(74) Lim, J.-S.; Aquino, M. A. S.; Sykes, A. G. *Inorg. Chem.* **1996**, *35*, 614−618.

(75) Vincent, J. B.; Crowder, M. W.; Averill, B. A. *J. Biol. Chem.* **1991**, *266*, 17737−17740.

(76) Wynne, C. J.; Hamilton, S. E.; Dionysius, D. A.; Beck, J. L.; de Jersey, J. *Arch. Biochem. Biophys.* **1995**, *319*, 133−141.